Morphology and Structure Engineering in Nanofiber Reactor: Tubular Hierarchical Integrated Networks Composed of Dual Phase Octahedral $CoMn_2O_4$/Carbon Nanofibers for Water Oxidation

*Han Zhu, Danni Yu, Songge Zhang, Jiawei Chen, Wenbo Wu, Meng Wan, Lina Wang, Ming Zhang, and Mingliang Du**

***1**D hollow nanostructures combine the advantages of enhanced surface-to-volume ratio, short transport lengths, and efficient 1D electron transport, which can provide more design ideas for the preparation of highly active oxygen evolution (OER) electrocatalysts. A unique architecture of dual-phase octahedral $CoMn_2O_4$/carbon hollow nanofibers has been prepared via a two-step heat-treatment process including preoxidation treatment and Ostwald ripening process. The hollow and porous structures provide interior void spaces, large exposed surfaces, and high contact areas between the nanofibers and electrolyte and the morphology can be engineered by adjusting the heating conditions. Due to the intimate electrical and chemical coupling between the oxide nanocrystals and integrated carbon, the dual-phase octahedral $CoMn_2O_4$/carbon hollow nanofibers exhibit excellent OER activity with overpotentials of 337 mV at current density of 10 mA cm^{-2} and Tafel slope of 82 mV dec^{-1}. This approach will lead to the new perception of design issue for the nanoarchitecture with fine morphology, structures, and excellent electrocatalytic activity.*

Dr. H. Zhu, Prof. M. L. Du
Key Laboratory of Synthetic and Biological Colloids
Ministry of Education
School of Chemical and Material Engineering
Jiangnan University
Wuxi 214122, P. R. China
E-mail: psduml@163.com

Dr. H. Zhu, D. N. Yu, S. G. Zhang, J. W. Chen, M. Wan, L. N. Wang, Dr. M. Zhang, Prof. M. L. Du
College of Materials and Textiles
Key Laboratory of Advanced Textile Materials and Manufacturing Technology of the Ministry of Education
Zhejiang Sci-Tech University
Hangzhou 310018, P. R. China

Dr. W. B. Wu
Department of Chemical and Biomolecular Engineering
National University of Singapore
4 Engineering Drive 4, 117585, Singapore

The ORCID identification number(s) for the author(s) of this article can be found under https://doi.org/10.1002/smll.201700468.

DOI: 10.1002/smll.201700468

1. Introduction

The severe global energy crisis has impelled the development of various types of sustainable energy conversion and storage systems.[1–3] In particular, hydrogen is considered as one of the promising alternative energy carrier to replace fossil fuels.[4,5] In order to achieve mass production of high-purity hydrogen with low cost and environment-friendly approach, electrochemical water splitting involving hydrogen evolution reaction (HER) and oxygen evolution reaction (OER) is considered to be an attractive way with zero emission.[4–7] However, the overall efficiency of water splitting is impeded by the sluggish kinetics of OER process (complicated multielectron transfer process), the considerable overpotential requirement, and the need for expensive noble metal catalysts, such as iridium and ruthenium oxides.[8–10]

Transition metal oxide based catalysts have drawn more attention to construct efficient and low-cost OER electrocatalysts, as metal species are widely regarded to be the active sites for electrochemical OER. Yu and co-workers have

designed a $Mn_3O_4/CoSe_2$ hybrid and achieve an overpotential of ≈450 mV at a current density of 10 mA cm^{-2} in KOH solution (pH 13).[11] Cheng and co-workers synthesized spinel type CoMnO nanocrystals and these catalyst manifest considerable catalytic activity toward the ORR/OER as a result of their high surface areas and abundant defects.[12] However, the use of state-of-the-art OER catalysts is complicated by the complex preparation approaches and low electrical conductivity of transition metal oxides, and the catalytic performance remains unsatisfactory. Therefore, the achievement of cost-effective OER catalysts with low overpotentials still require novel and sophisticated strategies for material design and synthesis. Recently, mixed-valent transition-metal oxides are potential candidates for OER catalysts due to their high abundance and outstanding redox stability in aqueous alkaline solutions.[13–15] Several cobalt-based spinel oxides such as Co_3O_4, $NiCo_2O_4$, $Co_3O_4/MnCo_2O_4$, and $MnCo_2O_4/CoMn_2O_4$ have been utilized in alkaline fuel cells and metal–air battery, water treatment, and glucose sensors.[13–17] The introduction of nanocarbons such as graphene and carbon nanotube can improve the electrocatalytic activity and stability of the oxides. Additionally, the variable valence states and structural flexibility of the spinel oxides offer great opportunities to fine-tune their catalytic properties.[18] Despite these efforts, researches on transition metal oxides/carbon OER catalysts are still quite challenging due to the limitations of synthetic strategies.

Nanoarchitecture with different dimensional nanostructures not only combine the advantages of various nanostructures but also compensate for the disadvantages of individual nanostructures, which can provide more design ideas for the preparation of highly active catalysts. Our groups have designed several nanoarchitecture integrated with 0D nanocrystals, 1D nanowires and nanotubes, and 2D nanoplates using electrospun nanofibers as host and reactor.[19–21] The electrospun nanofiber can form complex structures with metal ions and they exhibited different thermal behaviors during heat treatment, resulting in various nanostructures formation. 1D hollow nanostructures have been recognized as the most desirable material for applications in energy-related systems due to their enhanced surface-to-volume ratio, short transport lengths for ionic transport, and efficient 1D electron transport along the longitudinal direction.[22–24] Here, we have designed unique architectures of dual-phase octahedral $CoMn_2O_4$/carbon hollow nanofibers via a simple and convenient Ostwald ripening approach, including the advantages of hollow and porous structures, octahedral crystals with unique planes and carbon encapsulation. Previous reported inorganic hollow nanofibers are acquired by combining the sol–gel method and the electrospinning technique and the morphologies of the fibers depend on the competition between the evaporation rate and the process of phase separation. It is noted that the hollow nanofibers prepared by phase separation are only suitable for several transition metal oxides with simple components, such as TiO_2, ZnO, and so on.[25–27] Meanwhile, the hollow nanofibers usually consist of irregular nanoparticles and the morphology of the hollow nanofibers are difficult to control.[28–30]

In the present works, we have deliberately designed a two-step heat-treatment process including preoxidation treatment and Ostwald ripening process. In the first preoxidation treatment, the small $CoMn_2O_4$ nanocrystals induced outward mass migration on surfaces of nanofiber from the central part, leading to the formation of larger amount of small $CoMn_2O_4$ on surfaces of nanofibers. Then, during the subsequent high-temperature heat treatment, the small $CoMn_2O_4$ through Ostwald ripening mechanism formed hollow structures of the resultant fibers. The morphology and structure can be engineered by adjusting the heating conditions. The hollow and porous structures provide interior void spaces, large exposed surfaces, and high contact areas between the nanofibers and electrolyte. In addition, the integrated carbon constrict the growth of dual phase $CoMn_2O_4$ octahedron and play an important role as a physical buffer in enhancing the electrical conductivity and cycling durability. Due to the intimate electrical and chemical coupling between the oxide nanocrystals and carbon, the dual-phase octahedral $CoMn_2O_4$/carbon hollow nanowires exhibit excellent OER activity with overpotentials of 337 mV at current density of 10 mA cm^{-2} and Tafel slope of 82 mV dec^{-1}. The electrospun nanofiber reactor can allow both the dual phase $CoMn_2O_4$ crystals and carbon to be tailored individually prior to integration, thus enabling delicate optimization of the octahedral structure and electrocatalytic performance. This phenomenon has not been clearly observed in previous studies. This discovery can lead to the new perception of design issue for the nanoarchitecture with fine morphology, structures, and excellent electrocatalytic activity.

2. Results and Discussion

The morphology of the electrospun polyacrylonitrile nanofibers containing Co and Mn salts (CoMn/PAN) was observed by field-emission scanning electron microscopy (FE-SEM) (Figure S1, Supporting Information). The as-prepared CoMn/PAN exhibits typical fiber morphologies with smooth surfaces and 3D networks. The average diameter of the hybrid nanofibers is about 620 ± 60 nm. After the preoxidation process at 230 °C, as shown in **Figure 1**a, small binary CoMn oxides (CoMnO) nanoparticles (NPs) are uniformly and densely grown on the surfaces of oxidized carbon nanofibers (OCNFs). The CoMnO/OCNFs hybrid exhibit a well-organized 1D cylindrical morphology. The surface of CoMnO/OCNFs is rougher compared with that of the CoMn/PAN precursor nanofibers and pure CNFs (Figures S1 and S2, Supporting Information), owing to the growth of CoMnO NPs on OCNF surfaces. The average diameter of the CoMnO/OCNFs decrease to about 260 ± 45 nm, and while the average diameter of CoMnO NPs are about 4.4 ± 1.2 nm, as shown in Figure 1b,c. High resolution transmission electron microscope (HRTEM) image of the CoMnO/OCNFs clearly reveals the lattice fringe of CoMnO NPs with interplanar spacing about 2.5 Å, corresponding to the (311) planes of $CoMn_2O_4$ NPs. High-angle annular dark-field scanning TEM (HAADF-STEM) image (Figure 1d) also confirm the growth of $CoMn_2O_4$ NP on OCNFs surfaces.

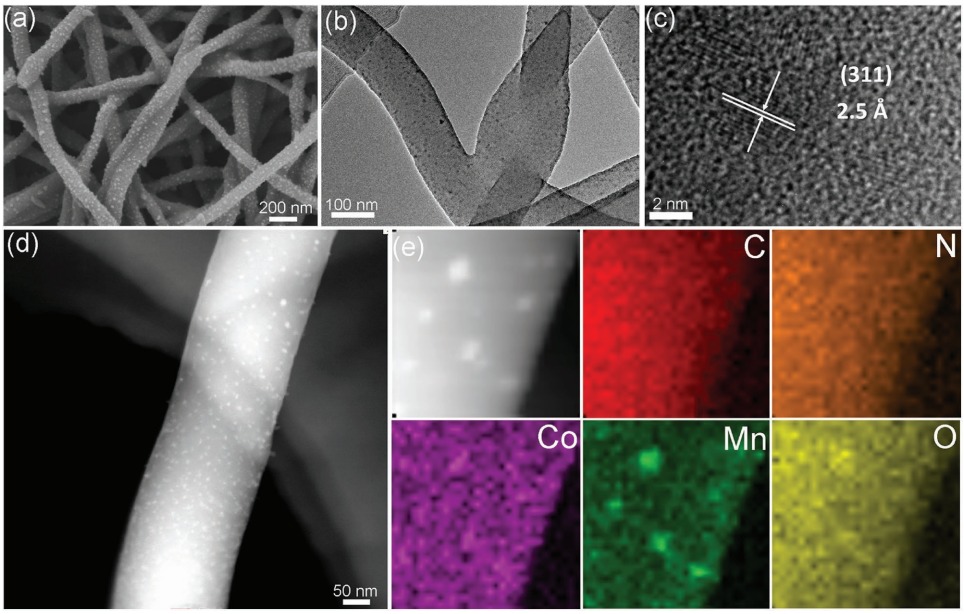

Figure 1. a) FE-SEM, b) TEM, c) HRTEM, d) HAADF-STEM, and e) STEM-EDX mapping images of the $CoMn_2O_4$/OCNFs hybrid prepared at 300 °C.

STEM-energy dispersive X-ray (STEM-EDX) mapping images (Figure 1e) of the $CoMn_2O_4$/OCNFs hybrid display uniform distribution of carbon, nitrogen, cobalt, manganese, and oxygen elements, indicating the formation of $CoMn_2O_4$ NPs. The X-ray diffraction (XRD) pattern of the $CoMn_2O_4$/OCNFs (Figure S3, Supporting Information) displays a serial of three distinct peaks located at 29.3°, 33.0°, 36.4°, 44.8°, 60.8°, and 65.2° correspond to the (112), (103), (121), (220), (224), and (040) planes, which are indexed to the tetragonal (Co, Mn)[Mn, Co]$_2O_4$ phase (ICSD 164369).[16] The other diffraction peaks located at 30.5°, 35.8°, 43.7°, and 63.3° correspond to the (220), (311), (400), and (440) planes, which are assigned to the cubic $(Mn_{1/3}Co_{2/3})$-$[Mn_{1/3}Co_{2/3}]_2O_4$ phase (ICSD 201314).[16] The XRD results indicate that the small $CoMn_2O_4$ NPs embedded in OCNFs are dual phase crystals. The broadband around 22.1° corresponds to the partial crystallinity of amorphous carbon.

After the subsequent calcination at 600 °C under atmosphere for 3 h, the original small $CoMn_2O_4$ NPs on surfaces of OCNFs formed hollow structures of the resultant fibers through the in situ Ostwald ripening. The resultant binary $CoMn_2O_4$ nanofibers exhibit a hierarchical structure and highly interconnected network. As shown in **Figure 2**c,d, the $CoMn_2O_4$ nanofibers displays hollow and porous structure, consisting of larger amounts of close packed octahedral $CoMn_2O_4$ NPs. The 1D porous $CoMn_2O_4$ nanofibers are closely connected with the adjacent ones, forming the continuous and interpenetrating 3D network. The size of the $CoMn_2O_4$ octahedral NPs ranges from 20 to 60 nm. Furthermore, some small pores on the surface of the hollow nanofibers can be observed due to the decomposition of polymer and formation of crystalline $CoMn_2O_4$ during calcination, which can directly increase the contact surfaces between the catalysts and electrolyte. As shown in Figure 2d, it can be clearly seen that the $CoMn_2O_4$ nanoparticles are octahedral morphology. The previously reported transition metal oxides nanofibers often mainly consist of small nanoparticles with irregular circle morphology.[22–27] Unlikely with them, the prepared $CoMn_2O_4$ hollow nanofibers possess octahedral morphology with abundant exposed (111) planes,[24–26] which provide more active sites for the electrocatalysis.

HRTEM image of the $CoMn_2O_4$ octahedron clearly exhibits two different lattice fringes, and the two different *d*-spacings of lattice fringes are 4.8 and 3.0 Å, corresponding to the (111) and (112) planes of dual phase $CoMn_2O_4$ octahedron. In addition, the fast Fourier transform (FFT) in the insets in Figure 2e also confirm existence of the dual phase of $CoMn_2O_4$ octahedron. It can be clearly seen that the $CoMn_2O_4$ octahedron were integrated by several layers of carbon, as shown in HRTEM in Figure 2e, indicating the carbon integrated structures. The STEM-EDX mapping images display three elements including cobalt, manganese, and oxygen. The element distribution of cobalt, manganese, and oxygen match well, demonstrating the formation of $CoMn_2O_4$ hollow nanofibers. In addition, the carbon element also has the same distribution morphology with the cobalt, manganese, and oxygen, demonstrating the carbon integrated structures. As shown in Figure 2l,m, the line scan EDX spectra illustrate the element distribution of Co, Mn, and O. The edges of the $CoMn_2O_4$ nanofibers possess the strongest intensity of Co, Mn, and O, indicating the successfully formation of hollow structures.

XRD and X-ray photoelectron spectroscopy (XPS) were used to further investigate the crystal structures and surface chemical states of the hollow nanofibers. **Figure 3**a shows the XRD patterns of the $CoMn_2O_4$ octahedron hollow nanofibers. The diffraction peaks located at 29.3°, 33.0°, 36.8°, 38.9°, 44.8°, 59.0°, and 65.4° correspond to the (112), (103), (121), (022), (220), (231), (224), and (040) planes, which are indexed to the tetragonal (Co, Mn)[Mn, Co]$_2O_4$ phase (ICSD 164369).[16] The other diffraction peaks located at 30.6°, 36.3°, 44.0°, 54.5°, 58.2°, and 63.7° correspond to the

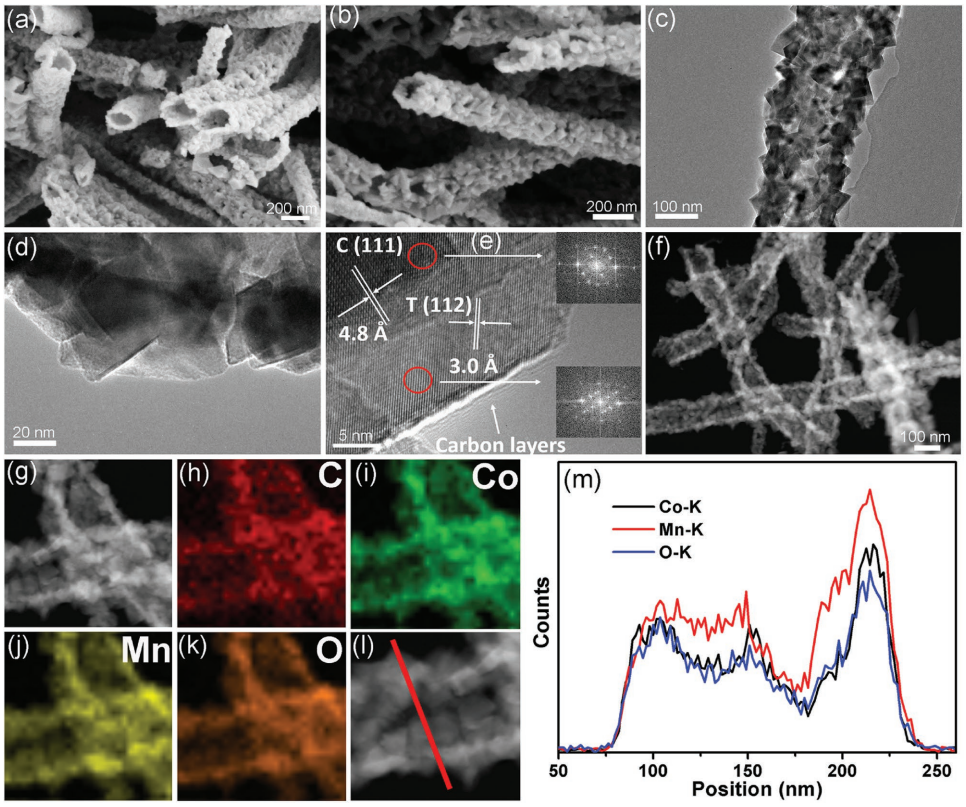

Figure 2. a,b) FE-SEM, c,d) TEM, and e) HRTEM images of the dual phase $CoMn_2O_4$/carbon octahedron hollow nanofibers. Insets are the corresponding FFT images of the dual phase $CoMn_2O_4$/carbon NP. f) HAADF-STEM, g–k) STEM-EDX mapping, and l,m) line scan EDX spectra of the dual phase $CoMn_2O_4$ octahedron hollow nanofibers.

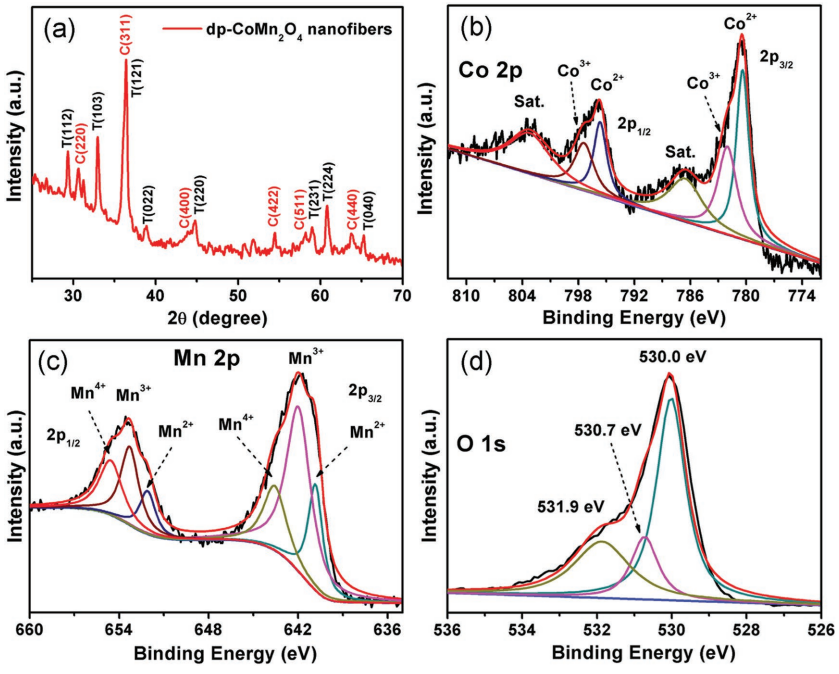

Figure 3. a) XRD pattern of the dual phase $CoMn_2O_4$/carbon octahedral hollow nanofibers. b) Co 2p, c) Mn 2p, and d) O 1s XPS spectra of dual phase $CoMn_2O_4$/carbon octahedral hollow nanofibers.

(220), (311), (400), (422), (511), and (440) planes, which are assigned to the cubic $(Mn_{1/3}Co_{2/3})$-$[Mn_{1/3}Co_{2/3}]_2O_4$ phase (ICSD 201314).[16] The XRD results indicate that the hollow $CoMn_2O_4$ octahedron nanofibers consist of two phase, the tetragonal (Co, Mn)[Mn, $Co]_2O_4$ phase and the cubic $(Mn_{1/3}Co_{2/3})$-$[Mn_{1/3}Co_{2/3}]_2O_4$ phase.

The thermal gravimetric analyzer (TGA) measurements of CoMn/PAN and pure PAN nanofibers under air were performed in order to measure weight losses of the nanofibers during the oxidative stabilization, determining the temperatures at which these processes are initiated and weight losses taking place in the nanofibers during these processes. Figures S4 and S5 (Supporting Information) show the TG curves of the as-spun CoMn/PAN and PAN nanofibers to simulate the calcination process in air at 10 °C min^{-1}. The pure PAN nanofibers obtain ≈5.6%, 16.3%, 23.4%, and 51.8% weight losses, which are present at 98.1, 331.4, 393.2, and 633.3 °C, respectively. These weight loss stages are attributed to the removal of the absorbed water and solvent, the cyclization and removal of volatiles, the partial decomposition of side chains of PAN, and the decomposition of PAN main chain. No further apparent weight loss is observed beyond 700 °C, and the residual material remains (≈2.6%), indicating that the PAN

cannot be completely removed. Figure S5 (Supporting Information) exhibits four stages and the CoMn/PAN nanofibers obtain ≈5.8%, 9.0%, 12.2%, and 62.9% weight losses, which are present at 67.3, 235.5, 319.5, and 410.2 °C, respectively. The weight loss below 200 °C (≈5.8%) is mainly due to the removal of the absorbed water and solvent. The second loss stage (≈9.0%) in the range of 200–300 °C is attributed to the decomposition of the Co and Mn nitrate in the gel fiber. The third stage (≈12.2%) from 300 to 400 °C is ascribed to the cyclization and partial decomposition of side chains of PAN. The forth stage from 400 to 500 °C displays the fast decomposition of PAN main chain (≈62.9%) and the formation of dual phase of $CoMn_2O_4$ crystals. No further apparent weight loss is observed beyond 500 °C, and the residual material (≈10.1%) is $CoMn_2O_4$ crystals and carbon.

Based on the TG results, with the thermal decomposition of Co and Mn nitrate at temperature above 200 °C, the metal oxide clusters start to form on the nanofiber surface where metal ions are in contact with ambient air. These metal oxides form small aggregates as the fiber diameter continues to decrease until they assemble into a rigid shell. With increased temperature, once the oxide shell forms, the fiber diameter stops decreasing, while the removal of additional PAN drives the remaining metal ions toward the surface. The oxidized PAN cannot completely removed at above 800 °C where the formation of oxide nanotubes is completed. As shown in the TEM images in Figure 2, the hollow $CoMn_2O_4$ are also integrated with carbon. This observation provides a useful guide in designing an appropriate heat treatment for reliably and reproducibly converting as-spun fibers to hollow nanofibers.

The XPS spectra were used to investigate the chemical states of dual phase $CoMn_2O_4$ hollow nanofibers. As shown in Figure S6 (Supporting Information), the XPS survey of $CoMn_2O_4$ hollow nanofibers exhibit C, Co, Mn, and O elements. The deconvoluted C 1s spectra (Figure S7, Supporting Information) displays two peaks with binding energies at 284.6 and 285.1 eV, corresponding to the C—C and C—N functional groups, respectively.[30,31] The high resolution Co 2p XPS spectrum shown in Figure 3b display the characteristic peaks located at 780.5 and 795.8 eV, which is attributed to the Co $2p_{3/2}$ and Co $2p_{1/2}$, thus confirming the presence of Co^{2+} ions. The other two peaks located at 782.1 and 797.5 eV with a spin–orbit splitting of 15.4 eV and satellite peaks corresponding to Co^{3+} ions.[16,19] In Figure 3c, the high resolution Mn 2p XPS spectra exhibit three pairs of peaks for Mn $2p_{3/2}$ and Mn $2p_{1/2}$. The binding energies located at 640.8 and 652.1 eV correspond to the Mn $2p_{3/2}$ and Mn $2p_{1/2}$ of Mn^{2+} ions. The two peaks located at 642.0 and 653.3 eV with a spin–orbit splitting of 11.3 eV of the Mn $2p_{3/2}$ and Mn $2p_{1/2}$ belong to the Mn^{3+} ions in spin type Mn oxides.[16,32,33] In addition, another two peaks at 643.6 and 654.6 eV are attributed to the Mn $2p_{3/2}$ and Mn $2p_{1/2}$ of Mn^{4+} ions. For the O 1s XPS spectra, the peaks at 530.0, 530.7, and 531.9 eV correspond to the O 1s signal of the lattice O^{2-} in $CoMn_2O_4$, the hydroxyl groups on the surface of $CoMn_2O_4$, and the residual oxygen-containing groups, respectively.[16,19,34] This result further indicates that the successfully formation of dual phase $CoMn_2O_4$ hollow nanofibers.

In order to investigate the confined effects of the PAN derived carbon nanofiber reactor for the formation of octahedral $CoMn_2O_4$ nanofibers, the $CoMn_2O_4$ nanofibers with different morphologies prepared at a series of temperatures. The above results in Figure 1 indicate that after the preoxidation process at 230 °C, the CoMn/PAN was converted into $CoMn_2O_4$/OCNFs. It was originated from reactions between the ambient oxygen and the organics decomposed from PAN and cobalt and manganese nitrate in PAN nanofibers during calcination.

Figure 4a,b displays the $CoMn_2O_4$/CNFs prepared at 400 °C under air condition after the preoxidation process. The $CoMn_2O_4$ nanocrystals with diameter in the range of 5–20 nm were encapsulated in the carbon nanofibers. At this temperature (400 °C), the carbon cannot be completely removed. With the temperature increased to 500 °C, the former $CoMn_2O_4$/OCNFs converted into $CoMn_2O_4$ nanofibers with tubular structures, as shown in Figure 4c,d. The $CoMn_2O_4$ nanofibers became hollow morphology and consist of small $CoMn_2O_4$ adjacent nanoparticles. The $CoMn_2O_4$ featured a single-walled hollow structure with relatively large particle sizes, and hence, a relatively rough surface morphology (Figure 4c,d). Figure 4e,f exhibits the porous $CoMn_2O_4$ hollow nanofiber prepared at 600 °C and the $CoMn_2O_4$ are not irregular particles but octahedral particle with dual phase. The hollow nanofiber can keep its networks and there are many small holes among the adjacent $CoMn_2O_4$ octahedron with exposed (111) planes, which are beneficial for the access of the electrolyte to the active cites. With further increased to 700 °C, the $CoMn_2O_4$ nanofibers with large grains were observed, and the nanofibers cannot maintain the hollow structures. Due to the high temperature, the small $CoMn_2O_4$ nanoparticles fused together and coalesced into larger sized particles (Figure 4g,h). Therefore, the increased treatment temperature leads to the morphology evolutions of hollow structures and $CoMn_2O_4$ octahedrons, suggesting the temperature sensitive structures.

XRD patterns of the dual phase $CoMn_2O_4$/carbon octahedral hollow nanofibers with increased heat temperatures are shown in **Figure 5**. The $CoMn_2O_4$/carbon nanofibers prepared at 400 °C exhibit several peaks, which can be indexed as dual phase $CoMn_2O_4$ crystals. With increased temperatures, more diffraction peaks emerge and become sharp, indicating the growth of $CoMn_2O_4$ crystal size. The $CoMn_2O_4$/carbon hollow nanofibers prepared at 600 °C possess more peaks than the others due to their unique octahedral morphology of the crystal particles. High temperature would result in the excessive growth of the crystal sizes, and also lead to the relative low exposed planes of dual phase $CoMn_2O_4$. XPS spectra were used to measure the atomic concentration of elements in the dual phase $CoMn_2O_4$ nanofibers prepared at different temperatures. As shown in **Table 1**, the atomic concentrations of the Co, Mn, and O elements increase with the increased temperature while the C element decrease. The atomic ratio of the CoMnO-400, CoMnO-500, CoMnO-600, and CoMnO-700 for Co:Mn:O:C are 1:1.51:6.1:21.7, 1:1.50:6.1:18.8, 1:1.51:6.0:9.0, and 1:1.51:6.1:4.9, respectively. The Co, Mn, and O ratio for all the samples is about 1:1.5:6.0, indicating

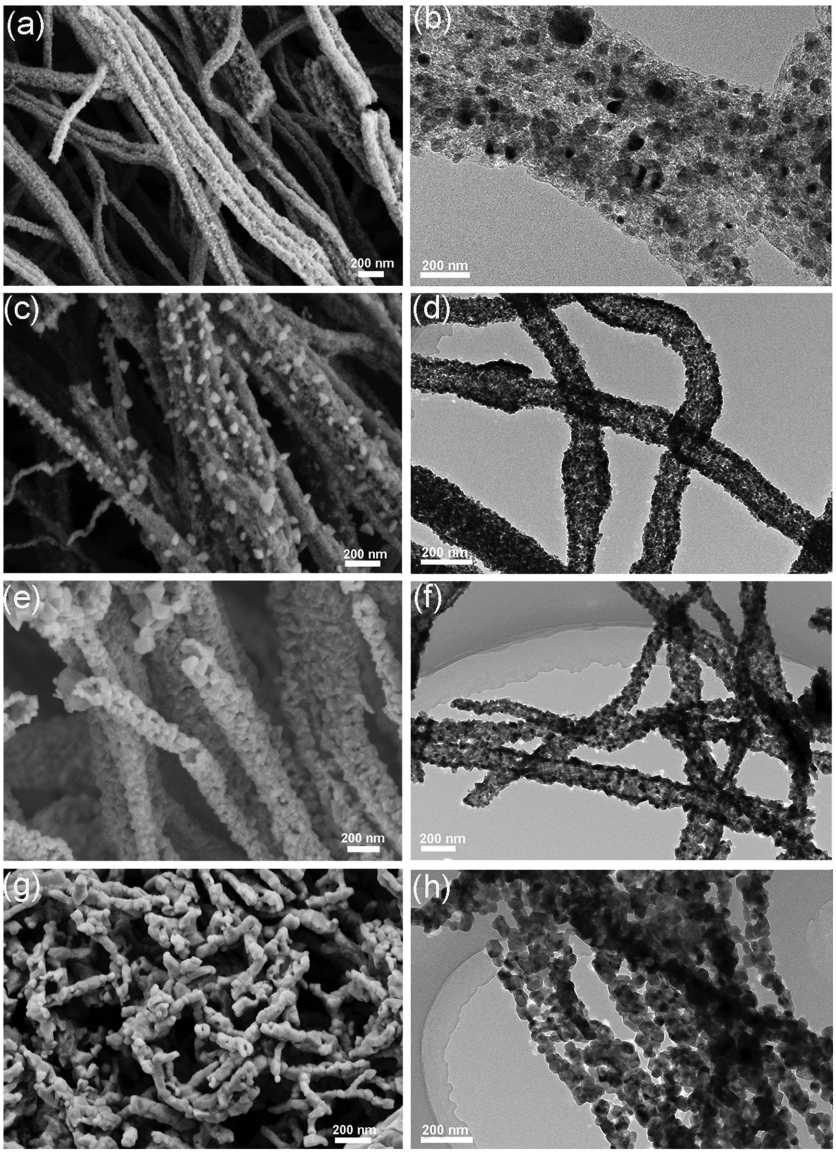

Figure 4. FE-SEM and TEM images of the morphology evolutions of the dual phase $CoMn_2O_4$/carbon octahedral hollow nanofibers with increased heat temperatures: a,b) 400 °C, c,d) 500 °C, e,f) 600 °C, and (g,h) 700 °C.

that the temperature of 400 °C could lead to the formation of the dual phase of the $CoMn_2O_4$ nanocrystals.

Unlikely with the previous reported inorganic fibers acquired by combining the sol-gel method and the electrospinning technique due to the phase separation,[25–27] this present approach is easily to produce hollow nanofibers with defined crystal planes due to the Ostwald ripening. The growth process of the dual-phase $CoMn_2O_4$ octahedral hollow nanofibers is illustrated in **Scheme 1**. The first procedure is preoxidation and it can lead to the formation of large amounts of small $CoMn_2O_4$ NPs on the surfaces of oxidized CNFs and the $CoMn_2O_4$ NPs indicate a decreasing concentration gradient from its surface to the center. Then, during the high-temperature heat treatment process, the larger sized $CoMn_2O_4$ NPs on OCNFs surfaces are essentially immobile while the small sized $CoMn_2O_4$ NPs in the central of OCNFs undergo an oriented mass transfer to the outer shell by a recrystallization process, due to the relative higher free energy and less stability of sized $CoMn_2O_4$ NPs than that of larger sized $CoMn_2O_4$ NPs.[35] Therefore, an interior space is created within the fibers and hollow tubular structures are formed. The CNF cannot be completely removed during the calcination and the remaining carbon is integrated closely with the formed $CoMn_2O_4$/carbon hollow nanofiber, supporting the fast charge transfer from the electrode. With precisely temperature control, the hollow structures and $CoMn_2O_4$ morphology can be adjusted. This synthetic approach can be applied to other systems which consist of combination of other transition metal cations, such as $CoFe_2O_4$ and $NiMn_2O_4$. **Figure 6** displays the morphologies of the as-prepared $CoFe_2O_4$ and $NiMn_2O_4$ hollow nanofibers. They both exhibit tubular hierarchical integrated networks, indicating that the Ostwald ripening approach has the good applicability to other systems.

Having thoroughly characterized the dual-phase $CoMn_2O_4$/carbon octahedral hollow nanofibers, we investigated the electrocatalytic activity of $CoMn_2O_4$/carbon nanofibers prepared at different temperatures (marked as CoMnO-400, CoMnO-500, CoMnO-600, and CoMnO-700) on glassy carbon electrode (GCE) for OER in alkaline media (1 M KOH) by using commercially 20 wt% IrO_2/C catalysts as reference. As shown in **Figure 7**a, the CoMnO-600 hollow nanofiber with octahedron morphology exhibit the highest catalytic activity with a low onset potential of 240 mV versus reversible

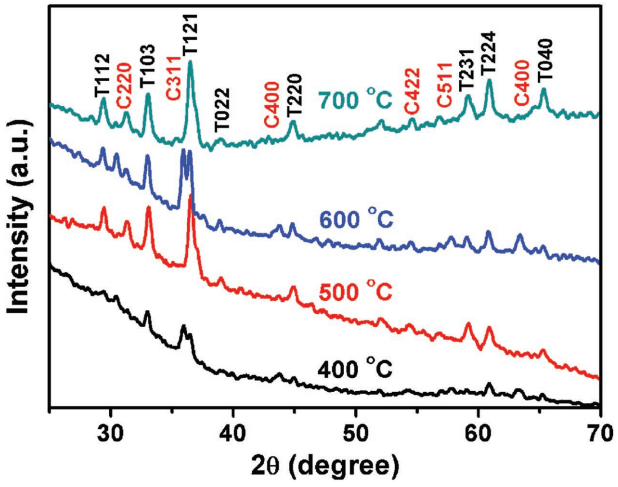

Figure 5. FE-SEM and TEM images of the morphology evolutions of the dual phase $MnCo_2O_4$/carbon octahedral hollow nanofibers with increased heat temperatures.

Table 1. The atomic concentration of the dual phase $CoMn_2O_4$ nanofibers prepared at different temperatures.

Samples	Co atomic concentrations [%]	Mn atomic concentrations [%]	O atomic concentrations [%]	C atomic concentrations [%]
CoMnO-400	3.25	4.9	19.83	70.4
CoMnO-500	3.59	5.35	21.89	67.69
CoMnO-600	5.66	8.54	33.72	51.06
CoMnO-700	6.94	10.61	42.58	34.07

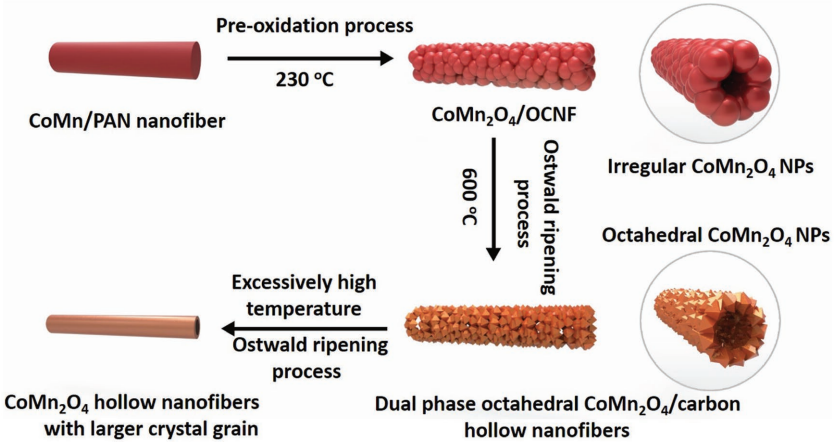

Scheme 1. FE-SEM and TEM images of the morphology evolutions of the dual phase $CoMn_2O_4$/carbon octahedral hollow nanofibers.

hydrogen electrode (RHE), above which the anodic current increases rapidly. The overpotential (η_{10}) at 10 mA cm^2 for CoMnO-400, CoMnO-500, CoMnO-600, CoMnO-700 are 393, 379, 337, and 363 mV, respectively, which are all smaller than the commercial IrO_2/C catalysts (Figure 7b).

This electrocatalytic activity of CoMnO-600 is superior to the behavior of non-noble electrocatalysts under the same conditions for the OER, such as the exfoliated NiCo layered double hydroxide nanosheets,[36] (η_{10} = 367 mV), Ni–Co double hydroxide nanocages[37] (η_{10} = 350 mV), irregularly shaped CoNi-P nanoparticles (CoNi(20:1)-ZIF-P (η_{10} = 348 mV),[38] $NiCo_2O_4$ hollow microcuboids (η_{10} = 420 mV),[39] and Ni/NiO_x-CNF (η_{10} = 420 mV).[40] Moreover, the electrocatalytic activity of the various catalysts were compared by recording their current densities at an overpotential of 400 mV, as shown in Figure 7c. The CoMnO-600 displays the highest current density of 40.96 mA cm^{-2}, which are higher than that for CoMnO-400 (15.2 mA cm^{-2}), CoMnO-500 (16.54 mA cm^{-2}), CoMnO-700 (26.65 mA cm^{-2}), and IrO_2/C (29.12 mA cm^{-2}). The Tafel slopes are derived from the polarization curves in Figure 7d to investigate the OER process. The corresponding Tafel slope of the CoMnO-600 catalysts is 82 mV dec^{-1}, is much lower than that of CoMnO-400 (124 mV dec^{-1}), CoMnO-500 (90 mV dec^{-1}), CoMnO-700 (88 mV dec^{-1}), and IrO_2/C (92 mV dec^{-1}), indicating that the hollow structure and octahedral morphology can deliver a much more favorable reaction kinetics and provide a remarkably increased OER rate with the increase of overpotentials.[34] The dual-phase $CoMn_2O_4$ octahedral hollow nanofibers obtain outstanding electrocatalytic performance as an efficient OER catalyst, including low overpotential, high current density, and low Tafel slope.

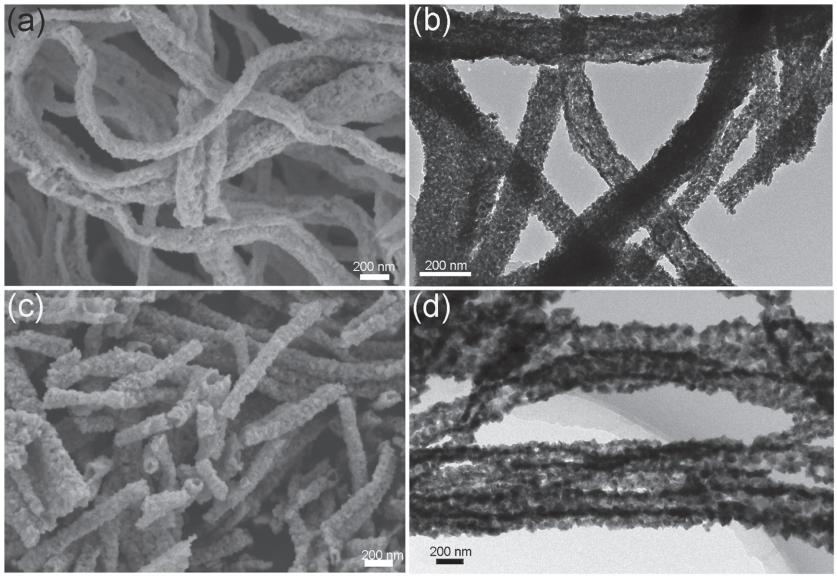

Figure 6. FE-SEM and TEM images of the as-prepared a,b) $CoFe_2O_4$ and c,d) $NiMn_2O_4$ through the Ostwald ripening approach.

Further kinetic insights about electrode process and charge transfer was obtained by electrochemical impedance spectroscopy (EIS) studies. All the measurements were conducted from 10^5 Hz to 0.01 Hz with an AC amplitude of 10 mV in 1.0 M KOH. Figure 7e shows the Nyquist plots of CoMnO samples at an overpotential of 420 mV. As expected, the CoMnO-600 exhibits a much smaller charge transfer resistance (R_{ct}) of 102 Ω (Figure 7f), which suggests that the CoMnO-600 has a much faster electron transfer than the other samples during the OER process. This could presumably be attributed to the unique porous architecture and mesoporous surfaces of octahedral $CoMn_2O_4$ chains in hollow nanofibers, which could render faster desorption of O_2 from active surface sites.

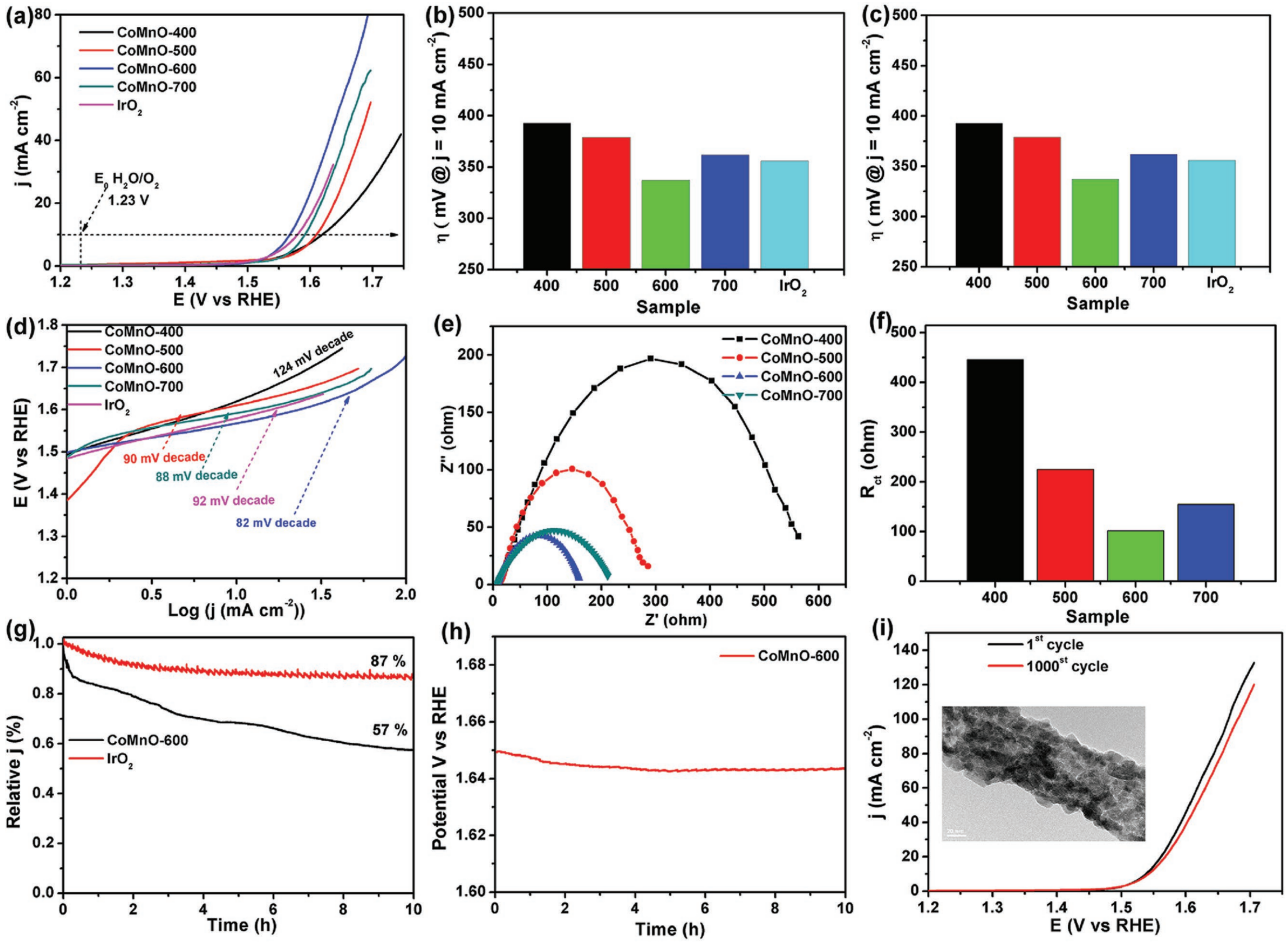

Figure 7. a) Polarization curves of the $CoMn_2O_4$/carbon hollow nanofibers catalysts prepared at different temperatures (CoMnO-400, CoMnO-500, CoMnO-600, and CoMnO-700) and commercial 20% IrO_2/C on GCE. (All tests were conducted in 1.0 M KOH.) b) Overpotentials of the corresponding various $CoMn_2O_4$ hollow nanofibers catalysts and commercial IrO_2/C at the current density of 10 mA cm^{-2}. c) Current density of the corresponding various $CoMn_2O_4$ hollow nanofibers catalysts and commercial IrO_2/C at overpotentials of 400 mV. d) The Tafel plots of the catalysts derived from the corresponding polarization curves. e) Nyquist plots of different catalysts recorded at an overpotential of 420 mV. f) The R_{ct} obtained on different catalysts. g) The chronoamperometric responses of the $CoMn_2O_4$ prepared at 600 °C (CoMnO-600) and commercial IrO_2/C for OER. h) A time-dependent profile of $CoMn_2O_4$ prepared at 600 °C at 1.65 V for 10 h. i) Polarization curves for CoMnO-600 on GCE initially (black) and after 1000 (red) CV sweeps.

To evaluate the stability of the CoMnO-600 for the OER in 1 M KOH, we tested the chronoamperometric responses of the CoMnO-600 and commercial IrO_2/C under continuous electrolysis for 10 h (Figure 7g). After 10 h, the current density of the CoMnO-600 catalysts can maintain 87%, which is much higher than that of IrO_2/C (57%), suggesting the superior stability of CoMnO-600 catalysts. The time-dependent of applied potentials for OER shows that the potentials remain stable over 10 h, further confirming the excellent long-term stability of CoMnO-600 (Figure 7h). Figure 7i indicate that the linear sweep voltammetry (LSV) curve of CoMnO-600 has only a little decrease after 1000 CV cycles, suggesting the superior operational stability in alkaline solution.

3. Conclusion

In summary, we have designed unique architectures of dual-phase octahedral $CoMn_2O_4$/carbon hollow nanofibers via a simple and convenient Ostwald ripening approach. The dual-phase octahedral $CoMn_2O_4$/carbon hollow nanofibers were prepared by a two-step heat-treatment process including preoxidation treatment and Ostwald ripening process. The morphology and structure can be engineered by adjusting the heating conditions. The hollow and porous structures provide interior void spaces, large exposed surfaces and high contact areas between the nanofibers and electrolyte. In addition, the integrated carbon constrict the growth of dual phase $CoMn_2O_4$ octahedron and play an important role as a physical buffer in enhancing the electrical conductivity and cycling durability. Due to the intimate electrical and chemical coupling between the oxide nanocrystals and carbon, the dual-phase octahedral $CoMn_2O_4$/carbon hollow nanowires exhibit excellent OER activity with overpotentials of 337 mV at current density of 10 mA cm^{-2} and Tafel slope of 82 mV dec^{-1}. This approach would lead to the new perception of design issue for the nanoarchitecture with

fine morphology, structures and excellent electrocatalytic activity.

4. Experimental Section

Preparation of the CoMn/PAN Nanofibers: In a typical procedure, 300 mg of cobalt nitrate and 300 mg manganese acetate were dissolved in 25 mL N,N-dimethylformamide (DMF) (contain 1.500 g PAN) solution. The above mixture was stirred vigorously at room temperature for 24 h and then transferred to a 10 mL plastic syringe with a 20-gauge blunt tip needle. For the electrospinning process, a high voltage of 18 kV and a flow rate of 0.6 mL h^{-1} were applied, with a distance of 15 cm between the needle and rotating grounded collector.

Preparation of the Dual-Phase $CoMn_2O_4$/Carbon Octahedron Hollow Nanofibers: The as-collected electrospun CoMn/PAN nanofibers were first placed into a home-built chemical vapor deposition system. The nanofibers membranes were first underwent heat treatment at 230 °C for 2 h in atmosphere and then at 300 °C for 3 h in an Ar atmosphere to obtain the binary Co and Mn oxides in oxidized carbon nanofibers (CoMnO/OCNFs). Afterward, the CoMnO/OCNFs hybrid nanofibers were kept at 600 °C for 4 h under atmosphere to achieve the dual-phase $CoMn_2O_4$ octahedron hollow nanofibers. The heating rate was kept at 1 °C min^{-1} for the whole experiments.

Characterization: The morphology and structure of the as-prepared samples were acquired by FESEM (Zeiss Supra 55VP), TEM (Model JEM-2010, JEOL), HAADF-STEM (Tecnai G2 F30S-Twin, Philips-FEI), STEM mapping, and line-scan EDX spectroscopy. XRD patterns were analyzed by a Bruker AXS D8 DISCOVER X-ray diffractometer with Cu Kα radiation ($\lambda = 1.5406$ Å) at a scanning rate of 0.02 2θ s^{-1} in the 2θ range of 10°–80°. Weight losses of the composite nanofibers in air environments were determined using a thermogravimetric analyzer (TA-Instruments TGA-Q500) heating from 25 to 800 °C (heating rate of 10 °C min^{-1}). X-ray photoelectron spectra of the products were recorded using an X-ray photoelectron spectrometer (Kratos Axis Ultra DLD) with an Al (mono) Kα source (1486.6 eV). The Al Kα source was operated at 15 kV and 10 mA.

Electrochemical Measurements: All electrochemical tests were performed at room temperature in a standard three-electrode system controlled by an Autolab potentiostat/galvanostat (Model PGSTAT302N) workstation. A carbon rod and a saturated calomel electrode (SCE) were used as the counter and reference electrode, respectively. In all measurements, the SCE reference electrode was calibrated with respect to the (E(RHE) = E(SCE) + 0.244 V). To prepare the working electrode, all samples were fixed in a Teflon electrode clamp and immersed in 1 M KOH. 4 mg of the catalyst was ultrasonically dispersed into the mixture of 1 mL Milli-Q water and 1 mL isopropanol. 20 µL of the catalyst dispersion (2.0 mg mL^{-1}) was then transferred onto the GCE (0.196 cm^2) via a controlled drop casting method. Following overnight solvent evaporation in air, a thin layer of Nafion solution (1.0 wt% water solution) was coated onto the electrode surface and then dried in air for 1 h. The performance of the catalysts was recorded by LSV at a scan rate of 2 mV s^{-1}. EIS was carried out at 1.6 V versus RHE over a frequency range from 10^{-2} to 10^6 Hz. All electrochemical measurements were performed without IR compensation.

Supporting Information

Supporting Information is available from the Wiley Online Library or from the author.

Acknowledgements

This study was supported by the National Natural Science Foundation of China (NSFC) (Grant Nos. 51373154 and 51573166), the MOE & SAFEA, and 111 Project (B13025).

Conflict of Interest

The authors declare no conflict of interest.

[1] H. I. Karunadasa, C. J. Chang, J. R. Long, *Nature* **2010**, *464*, 1329.
[2] B. Y. Xia, Y. Yan, N. Li, H. B. Wu, X. W. D. Lou, X. Wang, *Nat. Energy* **2016**, *1*, 15006.
[3] Q. L. Zhu, W. Xia, T. Akita, R. Zou, Q. Xu, *Adv. Mater.* **2016**, *28*, 6391.
[4] J. Li, G. Zhan, Y. Yu, L. Zhang, *Nat. Commun.* **2016**, *7*, 11480.
[5] D. Escalera-López, Y. Niu, J. Yin, K. Cooke, N. V. Rees, R. E. Palmer, *ACS Catal.* **2016**, *6*, 6008.
[6] X. J. Chua, J. Luxa, A. Y. S. Eng, S. M. Tan, Z. Sofer, M. Pumera, *ACS Catal.* **2016**, *6*, 5724.
[7] W. Zhou, J. Zhou, Y. Zhou, J. Lu, K. Zhou, L. Yang, Z. Tang, L. Li, S. Chen, *Chem. Mater.* **2015**, *27*, 2026.
[8] C. Tang, H. F. Wang, X. Chen, B. Q. Li, T. Z. Hou, B. Zhang, Q. Zhang, M. M. Titirici, F. Wei, *Adv. Mater.* **2016**, *28*, 6845.
[9] Q. Liu, Y. Wang, L. Dai, J. Yao, *Adv. Mater.* **2016**, *28*, 3000.
[10] B. Weng, F. Xu, C. Wang, W. Meng, C. R. Grice, Y. Yan, *Energy Environ. Sci.* **2017**, *10*, 121.
[11] M. R. Gao, Y. F. Xu, J. Jiang, Y. R. Zheng, S. H. Yu, *J. Am. Chem. Soc.* **2012**, *134*, 2930.
[12] F. Cheng, J. Shen, B. Peng, Y. Pan, Z. Tao, J. Chen, *Nat. Chem.* **2011**, *3*, 79.
[13] Z. Wang, S. Xiao, Y. An, X. Long, X. Zheng, X. Lu, Y. X. Tong, S. Yang, *ACS Appl. Mater. Interfaces* **2016**, *8*, 13348.
[14] C. Li, X. Han, F. Cheng, Y. Hu, C. Chen, J. Chen, *Nat. Commun.* **2015**, *6*, 7345.
[15] J. Du, C. Chen, F. Cheng, J. Chen, *Inorg. Chem.* **2015**, *54*, 5467.
[16] X. Ge, Y. Liu, F. T. Goh, T. A. Hor, Y. Zong, P. Xiao, Z. Zhang, S. H. Lim, B. Li, X. Wang, Z. Liu, *ACS Appl. Mater. Interfaces* **2014**, *6*, 12684.
[17] K. Zhang, X. Han, Z. Hu, X. Zhang, Z. Tao, J. Chen, *Chem. Soc. Rev.* **2015**, *44*, 699.
[18] Z. Wu, L. P. Sun, M. Yang, L. H. Huo, H. Zhao, J. C. Grenier, *J. Mater. Chem. A* **2016**, *4*, 13534.
[19] H. Zhu, L. Gu, D. Yu, Y. Sun, M. Wan, M. Zhang, L. Wang, L. Wang, W. Wu, J. Yao, M. Du, S. Guo, *Energy Environ. Sci.* **2017**, *10*, 321.
[20] H. Zhu, J. Zhang, R. Yanzhang, M. Du, Q. Wang, G. Gao, J. Wu, G. Wu, M. Zhang, B. Liu, J. Yao, X. Zhang, *Adv. Mater.* **2015**, *27*, 4752.

[21] H. Zhu, M. Du, M. Zhang, M. Zou, T. Yang, S. Wang, J. Yao, B. Guo, *Chem. Commun.* **2014**, *50*, 15435.
[22] G. H. An, D. Y. Lee, H. J. Ahn, *ACS Appl. Mater. Interfaces* **2016**, *8*, 19466.
[23] J. W. Jung, C. L. Lee, S. Yu, I. D. Kim, *J. Mater. Chem. A* **2016**, *4*, 703.
[24] S. M. Hwang, S. Y. Kim, J. G. Kim, K. J. Kim, J. W. Lee, M. S. Park, Y. J. Kim, M. Shahabuddin, Y. Yamauchi, J. H. Kim, *Nanoscale* **2015**, *7*, 8351.
[25] H. Han, T. Song, J. Y. Bae, L. F. Nazar, H. Kim, U. Paik, *Energy Environ. Sci.* **2011**, *4*, 4532.
[26] H. G. Wang, S. Yuan, D. L. Ma, X. B. Zhang, J. M. Yan, *Energy Environ. Sci.* **2015**, *8*, 1660.
[27] X. Zhang, V. Aravindan, P. S. Kumar, H. Liu, J. Sundaramurthy, S. Ramakrishna, S. Madhavi, *Nanoscale* **2013**, *5*, 5973.
[28] J. S. Cho, Y. C. Kang, *Small* **2015**, *11*, 4673.
[29] Y. J. Hong, J. S. Cho, Y. C. Kang, *Chem.-Eur. J.* **2015**, *21*, 18202.
[30] J. Chen, D. Yu, W. Liao, M. Zheng, L. Xiao, H. Zhu, M. Zhang, M. L. Du, J. Yao, *ACS Appl. Mater. Interfaces* **2016**, *8*, 18132.
[31] S. G. Kim, J. S. Lee, J. Jun, D. H. Shin, J. Jang, *ACS Appl. Mater. Interfaces* **2016**, *8*, 6602.
[32] X. He, F. Yin, Y. Li, H. Wang, J. Chen, Y. Wang, B. Chen, *ACS Appl. Mater. Interfaces* **2016**, *8*, 26740.
[33] F. Lai, Y. E. Miao, Y. Huang, T. S. Chung, T. Liu, *J. Phys. Chem. C* **2015**, *119*, 13442.
[34] Y. M. Chen, L. Yu, X. W. D. Lou, *Angew. Chem. Int. Ed.* **2016**, *55*, 5990.
[35] F. Z. Mou, J. G. Guan, Z. G. Sun, X. A. Fan, G. X. Tong, *J. Solid State Chem.* **2010**, *183*, 736.
[36] H. Liang, F. Meng, M. Cabán-Acevedo, L. Li, A. Forticaux, L. Xiu, Z. Wang, S. Jin, *Nano Lett.* **2015**, *15*, 1421.
[37] J. Nai, H. Yin, T. You, L. Zheng, J. Zhang, P. Wang, Z. Jin, Y. Tian, J. Liu, Z. Tang, L. Guo, *Adv. Energy Mater.* **2015**, *5*, 1401880.
[38] X. Xiao, C. T. He, S. Zhao, J. Li, W. Lin, Z. Yuan, Q. Zhang, S. Wang, L. Dai, D. Yu, *Energy Environ. Sci.* **2017**, *10*, 893.
[39] X. Gao, H. Zhang, Q. Li, X. Yu, Z. Hong, X. Zhang, C. Liang, Z. Lin, *Angew. Chem. Int. Ed.* **2016**, *55*, 6290.
[40] B. Li, S. W. Chien, X. Ge, J. Chai, X. Y. Goh, K. T. Nai, T. S. A. Hor, Z. Liu, Y. Zong, *Mater. Chem. Front.* **2017**, *1*, 677.

Received: February 10, 2017
Revised: April 5, 2017
Published online:

